Applied Physics A (2021) 127:483
https://doi.org/10.1007/s00339-021-04604-8

Applied Physics A
Materials Science & Processing

Electrocaloric properties of lead-free ferroelectric ceramic near room temperature

Hend Kacem[1] · Ah. Dhahri[2,3] · Mohamed Amara Gdaiem[1] · Z. Sassi[4] · L. Seveyrat[4] · L. Lebrun[4] · V. Perrin[4] · J. Dhahri[1]

Received: 6 March 2021 / Accepted: 15 May 2021 / Published online: 2 June 2021

Abstract
Nowadays, much attention is paid for developing lead-free ceramics, which can be utilized in the refrigeration domain. This communication provides a detailed description of the synthesis and characterization of a lead-free solid solution of $BaTi_{0.91}Sn_{0.09}O_3$. The X-ray diffraction analysis showed that the compound exhibits a single phase of tetragonal symmetry (P4mm (99)). The average crystallite size estimated using Scherrer's technique was found to be 122 nm. The microstructure or surface morphology of the sintered sample was investigated by using scanning electron microscopy. Based on mapping image, the sensitivity and spatial resolution of the different elements in our sample were improved. Analytical and simulation data for the electrocaloric effect in our sample were reported. A good electrocaloric strength ($\xi = \Delta T/\Delta E$) of $\xi = 0.171$ K mm/kV near the ferroelectric-paraelectric phase transition temperature was obtained. These values are very interesting when compared to those for other materials and show the possibility of using such lead-free ceramics for refrigeration domain.

Keywords Lead-free ceramic · Ferroelectric · Theoretical model · Electrocaloric effect · Entropy change · Heat capacity change

1 Introduction

The refrigeration market has grown considerably because of the constant expansion of the industry, rising living standards, and climate change [1]. This has resulted in a lack of control over consumer energy expenditure. It should be noted that the extensive use of refrigeration is a major factor of excessive energy consumption resulting in the depletion of non-renewable energy resources, which exacerbates the effect of global warming. Nowadays, the open debate is mainly focused on the energy transition towards a green development focused on protecting the environment, preserving human health and reducing global warming [2–4]. The necessity to improve energy performance has become a major concern for industrial and scientific communities. This fragment of innovation has, therefore, become under great pressure to produce more sustainable technological solutions predicated on promising cooling technologies. A few successful techniques have been developed. For example, the thermoelectric technique (Thomson or Peltier, Seebeck effect), solar sorption [1], as well as magnetocaloric (MC) [5–8] and electrocaloric (EC) cooling [9–13]. Compared to MC cooling, EC cooling main advantage is that the high electric fields necessary for the refrigeration cycle are less costly and much easier to produce than the magnetic fields necessary for MC refrigeration [1]. The electrocaloric effect (ECE) could be defined in adiabatic conditions by the change of temperature when an electric field is applied. In 2006, Mischenko et al. found a giant ECE in thin films $PbZr_{0.95}Ti_{0.05}O_3$ (PZT) [9]. The disadvantage of this type of material is that they are toxic and require high electric fields, which limits practical applications [14, 15]. So far,

✉ Hend Kacem
kacem.hend@gmail.com

✉ Mohamed Amara Gdaiem
gdaiem_mohamed@hotmail.fr

[1] Laboratoire de la Matière Condensée et des Nanosciences, Faculté Des Sciences de Monastir, Université de Monastir, LR11ES40, 5000 Monastir, Tunisie

[2] Physics Department, Faculty of Science and Humanities in Ad-Dawadmi, Shaqra University, Shaqra 11911, Saudi Arabia

[3] Laboratoire de Physique Appliqué, Faculté Des Sciences de Sfax, Université de Sfax, B.P. 1171, Sfax 3000, Tunisie

[4] INSA-LYON, LGEF, EA682, Université de Lyon, 69621 Villeurbanne, France

most inorganic materials with exceptional ECE are lead-based while lead-free ceramics, generally, have a lower ECE [1, 16]. Nevertheless, because of worldwide lead limitations, there is a pressing need to create environmentally-friendly materials [17–22]. This makes them attractive to further research in relation to widely used refrigeration technology based on gas compression. Among the lead-free EC materials are the prototypical $BaTiO_3$ (BT), which has a maximum ECE at high temperatures [16, 23–25]. To enhance their ferroelectric performance and adjust their Curie temperature (T_C), near room temperature, a transition strategy has been adopted by substitution at A (such as $Ca^{2+}$and Sr^{2+}), B (such as $Sn^{4+}$and Zr^{4+}) or in both sites [26–30]. It worth noting that the substitution of Ti^{4+} by Sn^{4+} in BT has also been an effective way to shift the T_C close to room temperature and also to induce various interesting properties in the dielectric behavior and sensor applications [31–33]. Thus, it is important to continue research to achieve a giant ECE in a lead-free material in ceramic form by applying a relatively small electric field near room temperature.

In this work, we present a detailed study of the structural, morphology and EC properties of $BaTi_{0.91}Sn_{0.09}O_3$ compound, which can be a suitable candidate as a working substance in refrigeration domain near room temperature. A phenomenological model for the simulation of the dependence of polarization on temperature variation under different applied electric fields is used for predicting the different EC parameters such as entropy (ΔS^E), relative cooling power (RCP), heat capacity ($\Delta C_{P,E}$), temperature changes (ΔT) and electrocaloric strength ξ.

2 Experimental Details

$BaTi_{0.91}Sn_{0.09}O_3$ polycrystalline sample was prepared by the solid-state reaction method. In this process, stoichiometric amounts of $BaCO_3$ (99.9% purity, Aldrich), TiO_2 (99.9% purity, Aldrich) and SnO_2 (99.9% purity, Aldrich) precursors were taken in the appropriate molar ratio. The powders were weighed according to the stoichiometric proportion of the following equation:

$$BaCO_3 + 0.91TiO_2 + 0.09SnO_2 \rightarrow BaTi_{0.91}Sn_{0.09}O_3 + \uparrow CO_2 \quad (1)$$

The initial powder was prepared by grinding the starting materials in ethanol with an agate mortar for 2 h. Then, it was calcined in two stages: at 900 °C for 24 h and at 1200 °C for 12 h. The obtained powder was again ground for 2 h and pressed into pellets. Subsequently, these pellets were sintered at 1400 °C for 2 h to get dense ceramic. Hence, the experiment density of our sample was equal to 5.7 g/cm^3. Figure 1 summarizes the schematic diagram of the synthesis procedure for $BaTi_{0.91}Sn_{0.09}O_3$.

X-ray diffraction (XRD) pattern of our sample was recorded on a Philips diffractometer using CuKα radiation ($\lambda = 1.54056$ Å). The microstructure was characterized by scanning electron microscopy (SEM) using a TS QUATA 250. In order to predict the ECE properties, we determined the change in polarization as a function of the electric field for the selected temperature using a current Keithley 428 amplifier and a high voltage amplifier TREK Model 20/20C. The entropy change values, under different

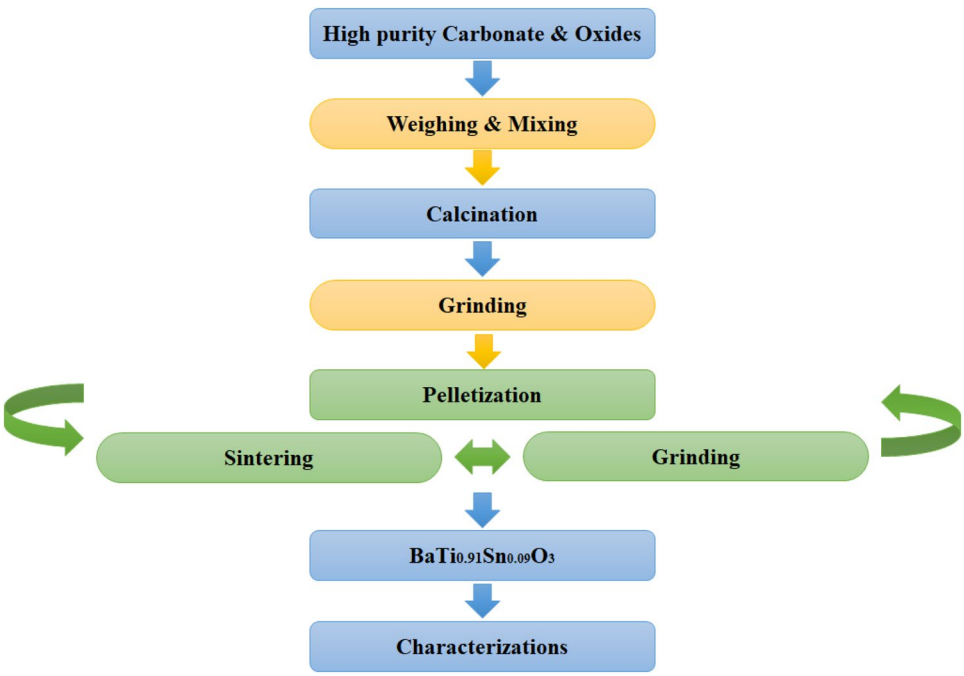

Fig. 1 Schematic diagram for synthesis of $BaTi_{0.91}Sn_{0.09}O_3$

applied electric field, (experimental data) are calculated, using the Maxwell approach [34]:

$$\Delta S_{\mathrm{E}} = \frac{1}{\rho}\int_{E_2}^{E_1}\left(\frac{\partial P}{\partial T}\right)_E \mathrm{d}E \tag{2}$$

where S, P, E, ρ and T are the entropy, polarization, applied electric field, mass density of the sample and the temperature of the system, respectively.

3 Results and discussion

3.1 Structural properties

To describe the structural properties of our sample, we carried out XRD analysis, at room temperature. Figure 2 shows the dependence of XRD patterns of BST ceramic. It crystallized in the tetragonal structure with P4mm (99) space group with cell parameters: $a=b=4.0187(0)$ Å and $c=4.0199(9)$ Å; $\alpha=\beta=\gamma=90°$.

Based on Debye Scherer's formula [35, 36] and Williamson–Hall (W–H) method [37, 38], the mean size of the crystallites of our ceramic was calculated, using the following equations:

$$D = \frac{k\lambda}{\beta\cos\theta} \tag{3}$$

$$\beta\cos\theta = 4\varepsilon\ \sin\theta + \frac{k}{D} \tag{4}$$

where k (=0.89), λ, β, θ, ε and D are, respectively, the shape factor, the wavelength of X-ray, the full width at half maximum (FWHM), the half of Bragg's angle, the strain in the lattice and the crystallite size. The values of D obtained using Debye Scherrer's formula and W–H method (inset of Fig. 2) were 129 and 151 nm, respectively. The difference of D values between the two methods is due to the lattice stress correction term in the calculations.

To better understand the morphology, the SEM image of our ceramic is shown in the inset (a′) of Fig. 3. The particles of our ceramic featured a relatively dense microstructure. Hence, the average particle size was estimated using ImageJ software. Then, we adjusted the data obtained with the log–normal function [35, 39]:

$$f(D) = \frac{1}{\sqrt{2\pi}\sigma D}\exp\left(-\frac{\ln\left(\frac{D}{D_0}\right)^2}{2\sigma^2}\right) \tag{5}$$

where σ and D_0 are, respectively, the data dispersions and the median diameter. The inset (a″) of Fig. 3 shows the dispersion histogram. The mean diameter $< D \geq D_0 \exp\left(\frac{\sigma^2}{2}\right)$ and stand deviation $\sigma_D = \langle D\rangle\left[\exp\sigma^2 - 1\right]^{\frac{1}{2}}$ were determined using the results obtained from the fit to Eq. (5). Therefore, the average grain size was found to be 0.6 µm. In order to confirm the existence of all elements present in our sample, the energy-dispersive X-ray (EDX) analysis was carried out. Figure 3a shows the appearance of characteristic peaks of these elements on the EDX spectrum, confirming the purity of our sample. In addition, Fig. 3b shows the composition dependence of element mapping. It was suggested that the distributions of the four elements are uniform, which improved the stability of the electrical properties.

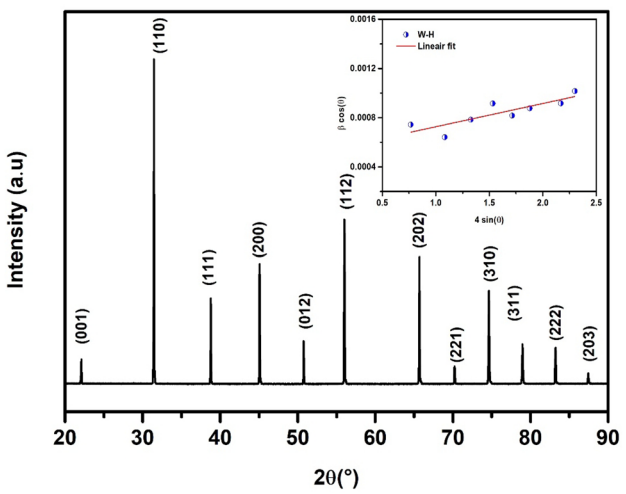

Fig. 2 XRD diffraction patterns of $BaTi_{0.91}Sn_{0.09}O_3$. The inset shows Williamson–Hall graph of our sample

3.2 ECE studies

3.2.1 Theoretical considerations

To determine EC properties, both the experimental and theoretical approaches were used. For the experimental evaluation, an approach based on polarization (P) data was applied (Eq. 2). However, for the theoretical investigation, a phenomenological model outlined in [40–42] is used. From this model, the variation of P versus temperature (T) and T_{C} can be defined as:

$$P = \left(\frac{P_{\mathrm{i}} - P_{\mathrm{f}}}{2}\right)\left[\tanh\left(A\left(T_{\mathrm{C}} - T\right)\right)\right] + BT + C \tag{6}$$

where;

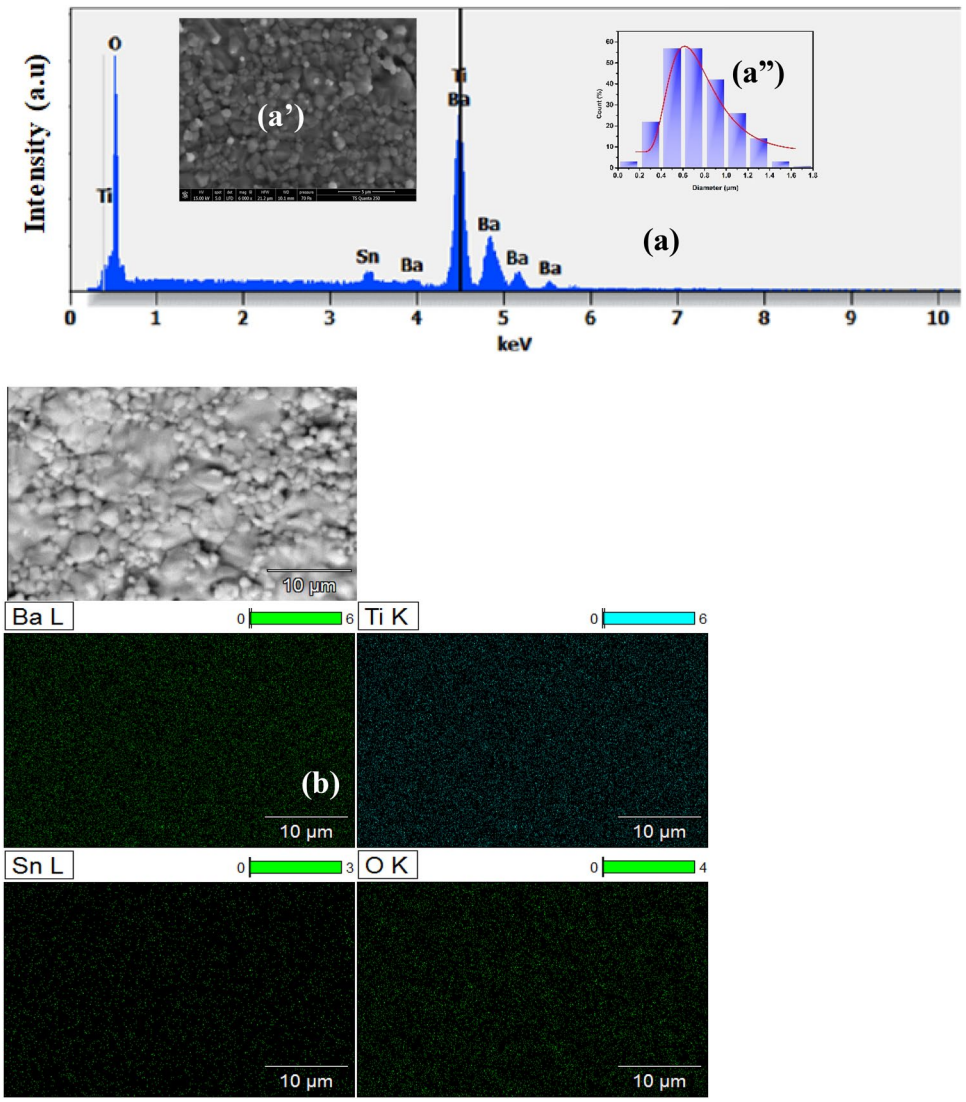

Fig. 3 **a** EDX analysis for $BaTi_{0.91}Sn_{0.09}O_3$ sample**.** Insets: **a″** of **a** shows the typical SEM and **a″** shows the histogram of the distribution of particles size. **b** EDX maps for Ba, Ti, Sn and O elements

- P_i/P_f are the initial/final values of P at ferroelectric (FE)–paraelectric (PE) transition, respectively, as shown in the inset (a) of Fig. 4.

$$A = \frac{2B - \left.\frac{dP}{dT}\right|_{T=T_c}}{P_i - P_f}$$

- B is P sensitivity $\frac{dP}{dT}$ at FE state before transition.

$$C = \frac{P_i + P_f}{2} - BT_c$$

From Eq. (6), the electrocaloric entropy change ΔS^E (Eq. 2), caused by the variation of the external electric field (E) from E_1 to E_2, can be rewritten as follows:

$$\Delta S^E = \left(-A\left(\frac{P_i - P_f}{2}\right)\mathrm{sech}^2\left(A\left(T_c - T\right)\right) + B\right)\frac{\Delta E}{\rho} \quad (7)$$

where ρ is the mass density of the sample.

At $T = T_C$, ΔS^E becomes maximum. So Eq. (7) may be written as follows:

$$\Delta S^E_{max} = \left(-A\left(\frac{P_i - P_f}{2}\right) + B\right)\frac{\Delta E}{\rho} \quad (8)$$

According to this model, a full width at half maximum can be calculated as follows:

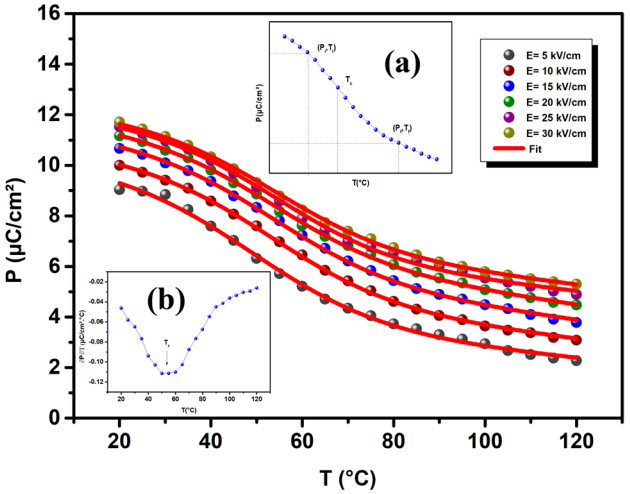

Fig. 4 Polarization versus temperature, under different electric field for $BaTi_{0.91}Sn_{0.09}O_3$ sample. The red lines are modeled results by Eq. (6) and symbols represent experimental data. The inset **a** shows the temperature dependence of polarization for $BaTi_{0.91}Sn_{0.09}O_3$ ceramic under constant electric field. The inset **b** is the plot of dP/dT versus T

$$\delta T_{\mathrm{FWHM}} = \frac{2}{A}\cosh^{-1}\left(\sqrt{\frac{2A\left(P_{\mathrm{i}}-P_{\mathrm{f}}\right)}{A\left(P_{\mathrm{i}}-P_{\mathrm{f}}\right)+2B}}\right) \tag{9}$$

Another very important parameter for refrigeration is the relative cooling power RCP, which presents the product of $\Delta S^{\mathrm{E}}_{\mathrm{Max}}$ and δT_{FWHM}. It is defined as:

$$\mathrm{RCP} = \Delta S^{\mathrm{E}}_{\mathrm{max}} \times \delta T_{\mathrm{FWHM}}$$

$$\mathrm{RCP} = \left(P_{\mathrm{i}} - P_{\mathrm{f}} - 2\frac{B}{A}\right)\frac{\Delta E}{\rho} \times \cosh^{-1}\left(\sqrt{\frac{2A\left(P_{\mathrm{i}}-P_{\mathrm{f}}\right)}{A\left(P_{\mathrm{i}}-P_{\mathrm{f}}\right)+2B}}\right) \tag{10}$$

A polarization-related change of heat capacity is given by:

$$\Delta C_{\mathrm{P,E}} = T\frac{\delta \Delta S^{\mathrm{E}}}{\delta T} \tag{11}$$

According to this phenomenological model, a change of heat capacity is given by:

$$\Delta C_{\mathrm{P,E}} = -2TA^2\left(\frac{P_{\mathrm{i}}-P_{\mathrm{f}}}{2}\right)\mathrm{sech}^2\left(A\left(T_{\mathrm{c}}-T\right)\right)\left(\tanh\left(A\left(T_{\mathrm{C}}-T\right)\right)\right)\frac{\Delta E}{\rho} \tag{12}$$

A temperature change of a polar system under adiabatic electric field variation from an initial value E_1 to final value E_2 can be written in the form:

$$\Delta T = -\frac{T}{C_{\mathrm{E}}\rho}\int_{E_1}^{E_2}\left(\frac{\partial P}{\partial T}\right)_E \mathrm{d}E = \frac{T}{C_{\mathrm{E}}\rho}\left[A\frac{(P_{\mathrm{i}}-P_{\mathrm{f}})}{2}\cdot\mathrm{sech}^2\left(A\left(T_c-T\right)\right)+B\right]\Delta E \tag{13}$$

C_{E} is a heat capacity at constant electric field.

3.2.2 Simulation

In order to apply the phenomenological model, numerical calculations were carried out with the parameters displayed in Table 1. The FE-PE transition temperature (T_{C}) was determined from the inflection point of dP/dT versus T (°C), as shown in the inset (b) of Fig. 4. Figure 4 shows P versus T for our sample under different electric fields (5–30 kV cm^{-1}). The symbols signify the experimental data and the red lines indicate the modeled data given by Eq. (6). It was found that these modeled data are consistent with the experimental data. Figure 5 shows the experimental entropy change data and their theoretical plot resulting from Eq. (7), at various applied electric fields. It appears that the results of the simulations agree well with the experimental data. It can also be noted that, for all applied electric fields and over the entire temperature range, the variation of ΔS^{E} is positive, which confirms the FE character [43]. From Fig. 5, ΔS^{E} increased sharply until reaching a peak near T_{C}. Hence, the values of $\Delta S^{\mathrm{E}}_{\mathrm{max}}$ are summarized in Table 2. Under an applied electric field $E = 30$ kV/cm, $\Delta S^{\mathrm{E}}_{\mathrm{max}}$ of our sample reached a value of 0.56 J kg^{-1} K^{-1}.

In the framework of EC refrigeration, it is essential to take into account two other parameters, having the same importance of $\Delta S^{\mathrm{E}}_{\mathrm{max}}$, namely RCP and δT_{FWHM}, which are defined in Eqs. 7 and 8, respectively. All EC parameters are recorded in Table 2, which are comparable to other works

Table 1 Model parameters for our sample, under different electric fields of 5–30 kV cm^{-1}

ΔE (kV cm^{-1})	T_{C} (°C)	P_{i} (μC cm^{-2})	P_{f} (μC cm^{-2})	A (μC cm^{-2} K^{-1})	B (μC cm^{-2} K^{-1})
5	49.13	8.358	2.375	0.03426	−0.01681
10	53.50	9.312	3.963	0.03569	−0.02016
15	53.92	9.683	4.721	0.03637	−0.02301
20	54.12	10.194	5.543	0.03716	−0.02407
25	54.16	10.708	5.601	0.036501	−0.01782
30	54.33	11.557	6.853	0.03702	−0.02019

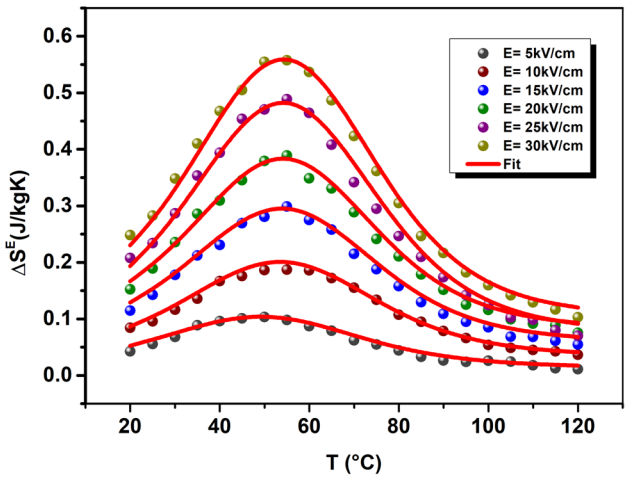

Fig. 5 ΔS_E as a function of temperature at different electric field, for $BaTi_{0.91}Sn_{0.09}O_3$ sample. The red line curves represent the modeled data results by Eq. (7) and symbols are the experimental data

such as 0.75 PMN-0.25 PT [44] and $Pb(Mg_{0.067}Nb_{0.133}Zr_{0.8})O_3$ [45]. Figure 6 shows the variation of $\Delta C_{P,E}$ as a function of the temperatures for different electric fields from 5 to 30 kV cm^{-1}, based on Eq. (12). In this figure, we can see that $\Delta C_{P,E}$ changed strongly from a negative to a positive value around T_C, which confirms FE behavior in our sample [40]. The obtained $\Delta C_{P,E}^{min}$ and $\Delta C_{P,E}^{max}$ values of our sample, under different electric fields, are listed in Table 2.

Using Eq. (13), Fig. 7a shows the experimental and theoretical curves of ΔT for our sample. It is obvious that the results of calculation are in good agreement with the experimental results. Also, it is clear that ΔT practically maintains the same behavior of ΔS^E. A maximum of ΔT was observed at around T_C, which is due to the great change in P with increasing T [46].

Furthermore, the EC strength ($\xi = \Delta T/\Delta E$) is generally used to predict the heating/cooling capacity of a material [44, 47]. The influence of the electric field and temperature on ξ for our samples shown in Fig. 7b. The variation of ξ versus T, under different electric fields, is similar to that of ΔT (Fig. 7a). Around room temperature, ξ reached a maximum value ($\xi_{RT} = 0.12$ K mm/kV) under an applied electric field equal to 5 kV/cm, which is higher than that of pure PZT ($\xi_{RT} = 0.02$ K mm/kV) [16]. Around T_C, the maximum of EC strength ($\xi_{max} = 0.171$ K mm/kV) of BST ceramic is significantly higher than other lead-free ferroelectrics such as SBT ($\xi_{max} = 0.083$) [48] and NBT ($\xi_{max} = 0.05$) [49].

The different obtained EC parameters for our sample are summarized in Table 3. We can note that our sample can be considered as potential candidate in the field of refrigeration thanks to its important ΔT and ξ values, compared to those observed in other materials [48, 50–62].

In general, to determinate the nature of the magnetic phase transition, the plots of the magnetic entropy change (ΔS_M) as function of T, under different applied magnetic fields, should collapse on a single curve with a second-order phase transition, which is suggested by Franco et al. [63, 64]. So by analogy with the MCE, the universal phenomenological $\Delta S'$ curve can be determined by the normalization of ΔS^E[65, 66]:

$$\Delta S' = \Delta S^E(T,E) / \Delta S^E_{max} \quad (14)$$

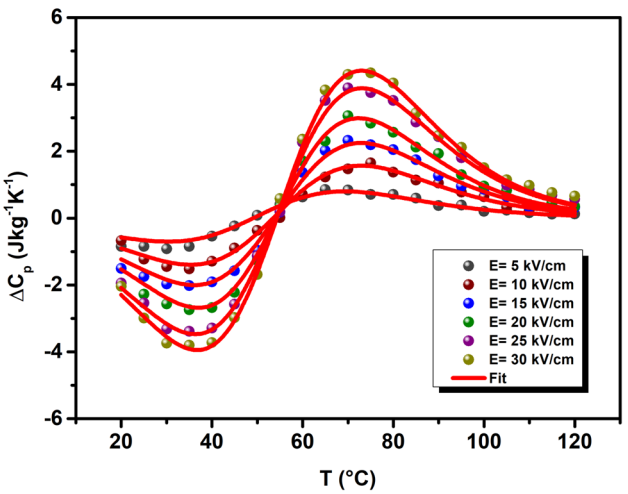

Fig. 6 Heat capacity changes versus temperature for $BaTi_{0.91}Sn_{0.09}O_3$ sample, obtained by Eq. (12) at different electric field

Table 2 Different values of EC properties for several applied electric fields of 5–30 kV/cm^{-1}

Sample	ΔE (kV cm^{-1})	T_C (°C)	δ_{TFWHM} (K)	ΔS^E_{max} (J kg^{-1} K^{-1})	RCP (J kg^{-1})	$\Delta C^{min}_{P,E}$ (J kg^{-1} K^{-1})	$\Delta C^{max}_{P,E}$ (J kg^{-1} K^{-1})
$BaTi_{0.91}Sn_{0.09}O_3$	5	49.13	50.4657	0.104679	7.40786	−0.7755	0.7514486
	10	53.50	44.49342	0.20140	8.96097	−1.439	1.531595
	15	53.92	47.223	0.2963	13.99127	−2.0462	2.194335
	20	54.12	45.98149	0.3856	17.73046	−2.7283	2.91578
	25	54.16	47.5222	0.4866	23.1243	−3.59047	3.817341
	30	54.33	46.8823	0.56	26.25409	−3.9928	4.39306

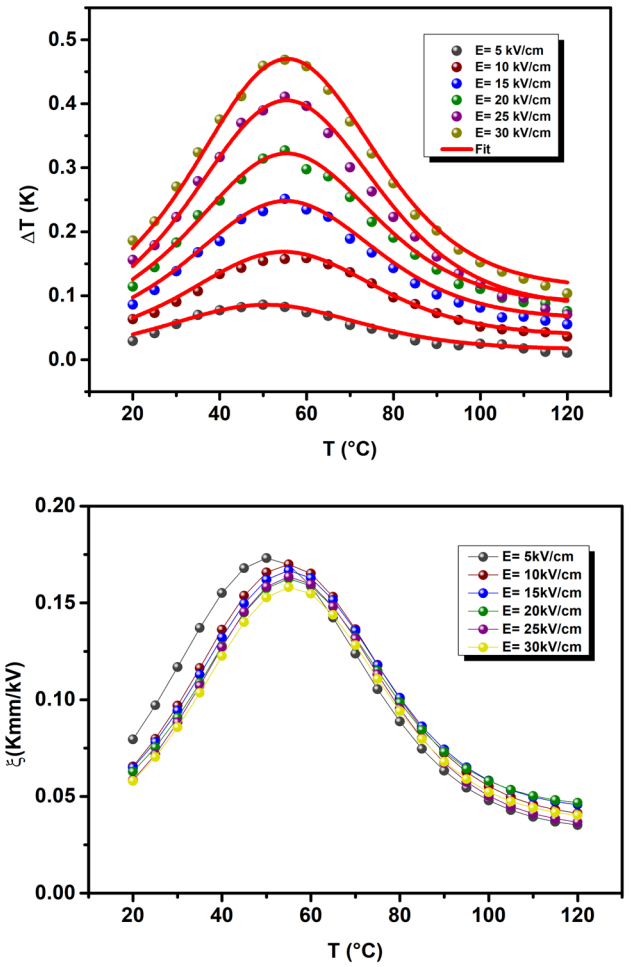

Fig. 7 **a** ΔT plotted as a function of temperature at different electric field, for $BaTi_{0.91}Sn_{0.09}O_3$ sample. The red line curves represent the modeled data results by Eq. (13) and symbols are the experimental data. **b** The temperature dependence of the electrocaloric strength ξ at different electric fields in the $BaTi_{0.91}Sn_{0.09}O_3$

Therefore, to construct the universal curve, it is important to resize the temperature axis, below and above T_C, by a new parameter on two clearly separated reference temperatures, represented by the following equation:

$$\theta = \begin{cases} \dfrac{T - T_C}{T_C - T_{r_1}} & T \le T_C \\ \dfrac{T - T_C}{T_{r_2} - T_C} & T \ge T_C \end{cases} \tag{15}$$

where θ, T_{r1} and T_{r2} are, respectively, the rescaled temperature and the temperatures lower and higher than T_C of each curve which should satisfy the relation $\Delta S^E\left(T_{r_{1,2}}\right) = \Delta S^E_{max}/2$.

The curves of $\Delta S'$ (θ) for the different applied electric fields are shown in Fig. 8. It is worth noting that all the data are dispersed on a single universal curve, which indicates that the transition in our sample is of a second order [67].

4 Conclusion

To sum up, $BaTi_{0.91}Sn_{0.09}O_3$ sample was prepared by solid-state method. XRD patterns showed that our sample crystallized in tetragonal structure with P4mm space group at room temperature. Based on mapping image, the sensitivity and spatial resolution of the different elements in our sample were improved. *P* versus *T* curves were adjusted at different electric fields and were used to calculate EC properties. Experimental and theoretical approaches were used to determine the EC properties. A good agreement of this model with the experimental data specifies the validity of this model under a variety of applied electric fields. Near room temperature, $BaTi_{0.91}Sn_{0.09}O_3$ sample displayed an important entropy change. The relative cooling power RCP was also analyzed. In addition, the maximum of EC strength (ξ_{max}) was found to be 0.171 K mm/kV around T_C, which is comparable to those obtained in the literature. These make our sample potential non-toxic candidate for cooling systems. According to the universal curve, we confirmed that the PE–FE phase transition observed for our sample is of second order.

Table 3 Comparison of the maximum electrocaloric strength (ξ_{max}) and ΔT for our sample with other ceramics

Material form	T_C (°C)	ΔT(K)	ΔE(kV/cm)	ξ (K mm/kV)	Refs
$BaTi_{0.91}Sn_{0.09}O_3$	49.13	0.09	5	0.171	Our work
$BaTi_{0.91}Sn_{0.09}O_3$	53.50	0.17	10	0.170	Our work
$BaTi_{0.91}Sn_{0.09}O_3$	53.92	0.25	15	0.167	Our work
$BaTi_{0.91}Sn_{0.09}O_3$	54.12	0.33	20	0.1623	Our work
$BaTi_{0.91}Sn_{0.09}O_3$	54.16	0.41	25	0.164	Our work
$BaTi_{0.91}Sn_{0.09}O_3$	54.33	0.47	30	0.158	Our work
$Ba_{0.8}Ca_{0.2}TiO_3$	125	0.12	8	0.15	[50]
$BaTi_{0.8}Zr_{0.2}O_3$	77	2.78	161	0.17	[51]
$BZr_{0.2}$ T-30$BCa_{0.3}$ T	60	0.3	20	0.15	[52]
BHT-40BST	61	0.34	30	0.11	[53]
$Ba_{0.97}Ce_{0.03}Ti_{0.99}Mn_{0.01}O_3$	55	0.41	30	0.14	[54]
$Ba_{0.865}Ca_{0.135}Zr_{0.1089}Ti_{0.8811}Fe_{0.01}O_3$	74	0.45	30	0.15	[55]
$Ba_{0.85}Ca_{0.15}Zr_{0.1}Ti_{0.9}O_3 + 0.004CuO$	110	0.09	15.3	0.06	[56]
$Pb(Zr_{0.43}Sn_{0.43}Ti_{0.14})O_3$	170	0.27	30	0.09	[57]
$(PbZrO_3)0.71$-$(BaTiO_3)_{0.29}$	25	0.15	20	0.08	[57]
$BaTiO_3$	130	0.78	55	0.142	[58]
$Ba_{0.7}Sr_{0.3}TiO_3$	40	0.67	40	0.16	[59]
$Ba_{0.85}Ca_{0.15}Zr_{0.1}Ti_{0.9}O_3$	97	0.40	21.5	0.186	[60]
P(VDF–TrFE) 55/45	80	12.6	209	0.06	[61]
$SrBi_2Ta_2O_9$	288	4.93	60	0.08	[48]
$Gd_{0.02}Na_{0.5}Bi_{0.48}TiO_3$	97	0.75	90	0.083	[62]

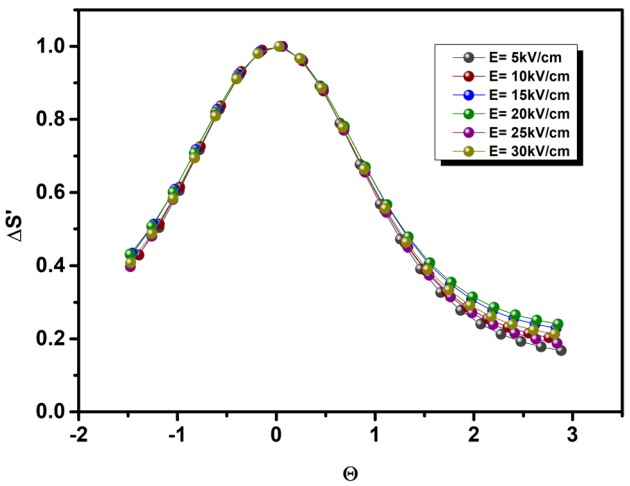

Fig. 8 $\Delta S'$ versus Θ for $BaTi_{0.91}Sn_{0.09}O_3$ sample, under different electric field

References

1. M. Valant, Electrocaloric materials for future solid-state refrigeration technologies. Prog. Mater. Sci. **57**(6), 980–1009 (2012). https://doi.org/10.1016/j.pmatsci.2012.02.001
2. S.K. Patel, B. Kuriachen, N. Kumar, R. Nateriya, The slurry abrasive wear behaviour and microstructural analysis of A2024-SiC-$ZrSiO_4$ metal matrix composite. Ceram. Int. **44**(6), 6426–6432 (2018). https://doi.org/10.1016/j.ceramint.2018.01.037
3. N. Fortas, A. Belkahla, S. Ouyahia, J. Dhahri, E.K. Hlil, K. Taibi, Effect of Ni substitution on the structural, magnetic and magnetocaloric properties of Zn Ni Mg Fe O (x= 0, 0.125 and 0.250) manganite. Solid State Sciences, **101**, 106137 (2020). https://doi.org/10.1016/j.solidstatesciences.2020.106137
4. X. Moya, S. Kar-Narayan, N.D. Mathur, Caloric materials near ferroic phase transitions. Nat. Mater. **13**(5), 439–450 (2014). https://doi.org/10.1038/nmat3951
5. L. Shebanovs, K. Borman, W.N. Lawless, A. Kalvane, Electrocaloric effect in some perovskite ferroelectric ceramics and multilayer capacitors. Ferroelectrics **273**(1), 137–142 (2002). https://doi.org/10.1080/00150190211761
6. M. Tishin, Y.I. Spichkin, *The Magnetoelectric Effect and Its Applications* (Institute of Physics Publishing, Philadelphia, 2003).
7. N. Kumar, A. Shukla, N. Kumar, R.N.P. Choudhary, Studies of structural, ferroelectric, magnetic and electrical characteristics of Bi (Fe1−xNdx) O3 (x= 0.05, 0.10, 0.15) multiferroics. J. Mater. Sci. Mater. Electron. **32**(5), 5870–5885 (2021). https://doi.org/10.1007/s10854-021-05308-8
8. N. Kumar, A. Shukla, R.N.P. Choudhary, Structural, electrical and magnetic characteristics of Ni/Ti modified $BiFeO_3$ lead free multiferroic material. J. Mater. Sci. Mater. Electron. **28**(9), 6673–6684 (2017). https://doi.org/10.1007/s10854-017-6359-y
9. A.S. Mischenko, Q. Zhang, J.F. Scott, R.W. Whatmore, N.D. Mathur, Giant electrocaloric effect in thin-film $PbZr_{0.95}Ti_{0.05}O_3$. Science **311**(5765), 1270–1271 (2006). https://doi.org/10.1126/science.1123811
10. H.J. Ye, X.S. Qian, D.Y. Jeong, S. Zhang, Y. Zhou, W.Z. Shao, L. Zhen, Q.M. Zhang, Giant electrocaloric effect in $BaZr_{0.2}Ti_{0.8}O_3$ thick film. Appl. Phys. Lett. **105**(15), 152908 (2014). https://doi.org/10.1063/1.4898599
11. X.S. Qian, S.G. Lu, X. Li, H. Gu, L.C. Chien, Q. Zhang, Large electrocaloric effect in a dielectric liquid possessing a large dielectric anisotropy near the isotropic–nematic transition.

Adv. Funct. Mater. **23**(22), 2894–2898 (2013). https://doi.org/10.1002/adfm.201202686
12. D. Matsunami, A. Fujita, Electrocaloric effect of metal-insulator transition in VO_2. Appl. Phys. Lett. **106**(4), 042901 (2015). https://doi.org/10.1063/1.4906801
13. N. Kumar, A. Shukla, N. Kumar, S. Sahoo, S. Hajra, R.N.P. Choudhary, Structural, electrical and ferroelectric characteristics of $Bi(Fe_{0.9}La_{0.1})O_3$. Ceram. Int. **44**(17), 21330–21337 (2018). https://doi.org/10.1016/j.ceramint.2018.08.185
14. S.G. Lu, B. Rožič, Q.M. Zhang, Z. Kutnjak, R. Pirc, M. Lin, X. Li, L. Gorny, Comparison of directly and indirectly measured electrocaloric effect in relaxor ferroelectric polymers. Appl. Phys. Lett. **97**(20), 202901 (2010). https://doi.org/10.1063/1.3514255
15. T.M. Correia, J.S. Young, R.W. Whatmore, J.F. Scott, N.D. Mathur, Q. Zhang, Investigation of the electrocaloric effect in a $PbMg_{2/3}Nb_{1/3}O_3$-$PbTiO_3$ relaxor thin film. Appl. Phys. Lett. **95**(18), 182904 (2009). https://doi.org/10.1063/1.3257695
16. G. Singh, V.S. Tiwari, P.K. Gupta, Electro-caloric effect in $(Ba_{1-x}Ca_x)(Zr_{0.05}Ti_{0.95})O_3$: a lead-free ferroelectric material. Appl. Phys. Lett. **103**(20), 202903 (2013). https://doi.org/10.1063/1.4829635
17. N. Kumar, A. Shukla, R.N.P. Choudhary, Development of lead-free multifunctional materials $Bi(Co_{0.45}Ti_{0.45}Fe_{0.10})O_3$. Prog. Nat. Sci. Mater. Int. **28**(3), 308–314 (2018). https://doi.org/10.1016/j.pnsc.2018.01.012
18. N. Kumar, A. Shukla, N. Kumar, R.N.P. Choudhary, A. Kumar, Structural, electrical, and multiferroic characteristics of lead-free multiferroic: $Bi(Co_{0.5}Ti_{0.5})O_3$–$BiFeO_3$ solid solution. RSC Adv. **8**(64), 36939–36950 (2018). https://doi.org/10.1039/C8RA02306A
19. H. Tang, X.G. Tang, M.D. Li, Q.X. Liu, Y.P. Jiang, Pyroelectric energy harvesting capabilities and electrocaloric effect in lead-free $Sr_xBa_{1-x}Nb_2O_6$ ferroelectric ceramics. J. Alloys Compd. **791**, 1038–1045 (2019). https://doi.org/10.1016/j.jallcom.2019.03.385
20. J. Koruza, B. Rožič, G. Cordoyiannis, B. Malič, Z. Kutnjak, Large electrocaloric effect in lead-free $K_{0.5}Na_{0.5}NbO_3$-$SrTiO_3$ ceramics. Appl. Phys. Lett. **106**(20), 202905 (2015). https://doi.org/10.1063/1.4921744
21. X. Jiang, L. Luo, B. Wang, W. Li, H. Chen, Electrocaloric effect based on the depolarization transition in (1–x) $Bi_{0.5}Na_{0.5}TiO_{3-x}KNbO_3$ lead-free ceramics. Ceram. Int. **40**(2), 2627–2634 (2014). https://doi.org/10.1016/j.ceramint.2013.10.066
22. N. Kumar, A. Shukla, Processing and characterization of Cd/Ti co-substituted $BiFeO_3$ nanoceramics. Int. J. Mod. Phys. B **32**(19), 1840069 (2018). https://doi.org/10.1142/S0217979218400696
23. Y. Liu, I.C. Infante, X. Lou, D.C. Lupascu, B. Dkhil, Giant mechanically-mediated electrocaloric effect in ultrathin ferroelectric capacitors at room temperature. Appl. Phys. Lett. **104**(1), 012907 (2014). https://doi.org/10.1063/1.4861456
24. Y. Bai, G. Zheng, S. Shi, Direct measurement of giant electrocaloric effect in $BaTiO_3$ multilayer thick film structure beyond theoretical prediction. Appl. Phys. Lett. **96**(19), 192902 (2010). https://doi.org/10.1063/1.3430045
25. X. Moya, E. Stern-Taulats, S. Crossley, D. González-Alonso, S. Kar-Narayan, A. Planes, L. Mañosa, N.D. Mathur, Giant electrocaloric strength in single-crystal $BaTiO_3$. Adv. Mater. **25**(9), 1360–1365 (2013). https://doi.org/10.1002/adma.201203823
26. X.Q. Liu, T.T. Chen, M.S. Fu, Y.J. Wu, X.M. Chen, Electrocaloric effects in spark plasma sintered $Ba_{0.7}Sr_{0.3}TiO_3$-based ceramics: effects of domain sizes and phase constitution. Ceram. Int. **40**(7), 11269–11276 (2014). https://doi.org/10.1016/j.ceramint.2014.03.175
27. X.S. Qian, H.J. Ye, Y.T. Zhang, H. Gu, X. Li, C.A. Randall, Q.M. Zhang, Giant electrocaloric response over a broad temperature range in modified $BaTiO_3$ ceramics. Adv. Funct. Mater. **24**(9), 1300–1305 (2014). https://doi.org/10.1002/adfm.201302386
28. Y. Bai, X. Han, K. Ding, L.J. Qiao, Combined effects of diffuse phase transition and microstructure on the electrocaloric effect in $Ba_{1-x}Sr_xTiO_3$ ceramics. Appl. Phys. Lett. **103**(16), 162902 (2013). https://doi.org/10.1063/1.4825266
29. L. Jin, R. Huo, R. Guo, F. Li, D. Wang, Y. Tian, Q. Hu, X. Wei, Z. He, Y. Yan, G. Liu, Diffuse phase transitions and giant electrostrictive coefficients in lead-free Fe^{3+}-doped 0.5 $Ba(Zr_{0.2}Ti_{0.8})O_{3-0.5}(Ba_{0.7}Ca_{0.3})$ TiO_3 ferroelectric ceramics. ACS Appl. Mater. Interfaces **8**(45), 31109–31119 (2016). https://doi.org/10.1021/acsami.6b08879
30. K.N.D.K. Muhsen, R.A.M. Osman, M.S. Idris, The effects of Ca, Zr and Sn substitutions into a ternary system of $BaTiO_3$–$BaSnO_3$–$BaZrO_3$ towards its dielectric and piezoelectric properties: a review. J. Mater. Sci. Mater. Electron. (2020). https://doi.org/10.1007/s10854-020-03756-2
31. K.N.D.K. Muhsen, R.A.M. Osman, M.S. Idris, M.H.H. Jumali, N.H.B. Jamil, Enhancing the dielectric properties of $(Ba_{0.85}Ca_{0.15})(SnxZr_{0.10-x}Ti_{0.90})O_3$ lead-free ceramics by stannum substitution. J. Mater. Sci. Mater. Electron. **30**(23), 20654–20664 (2019). https://doi.org/10.1007/s10854-019-02431-5
32. H. Kaddoussi, Y. Gagou, A. Lahmar, J. Belhadi, B. Allouche, J.L. Dellis, M. Courty, H. Khemakhem, M. El Marssi, Room temperature electro-caloric effect in lead-free $Ba(Zr_{0.1}Ti_{0.9})_{1-x}Sn_xO_3$ (x= 0, x= 0.075) ceramics. Solid State Commun. **201**, 64–67 (2015). https://doi.org/10.1016/j.ssc.2014.10.003
33. N. Baskaran, H. Chang, Effect of Sn doping on the phase transformation properties of ferroelectric $BaTiO_3$. J. Mater. Sci. Mater. Electron. **12**(9), 527–531 (2001). https://doi.org/10.1023/A:1012453526652
34. J.F. Scott, Electrocaloric materials. Ann. Rev. Mater. Res. **41**, 229–240 (2011). https://doi.org/10.1146/annurev-matsci-062910-100341
35. A. Dhahri, H. Kacem, J. Dhahri, Effect of La^{3+} substitution on the physical properties of $CaTiO_{3-0.15}KNbO_3$-based lead-free ceramics. Appl. Phys. A **126**(8), 1–10 (2020). https://doi.org/10.1007/s00339-020-03789-8
36. N. Kumar, A. Shukla, R.N.P. Choudhary, Structural, dielectric, electrical and magnetic characteristics of lead-free multiferroic: $Bi(Cd_{0.5}Ti_{0.5})O_3BiFeO_3$ solid solution. J. Alloys Compd. **747**, 895–904 (2018). https://doi.org/10.1016/j.jallcom.2018.03.114
37. G.K. Williamson, W.H. Hall, X-ray line broadening from filed aluminium and wolfram. Acta Metall. **1**(1), 22–31 (1953). https://doi.org/10.1016/0001-6160(53)90006-6
38. N. Kumar, A. Shukla, R.N.P. Choudhary, Structural, electrical and magnetic properties of (Cd, Ti) modified $BiFeO_3$. Phys. Lett. A **381**(33), 2721–2730 (2017). https://doi.org/10.1016/j.physleta.2017.06.012
39. M.H. Ehsani, T. Raoufi, F.S. Razavi, Impact of Gd ion substitution on the magneto-caloric effect of $La_{0.6-x}Gd_xSr_{0.4}MnO_3$ (x= 0, 0.0125, 0.05, 0.10) manganites. J. Magn. Magn. Mater. **475**, 484–492 (2019). https://doi.org/10.1016/j.jmmm.2018.11.131
40. M.A. Hamad, Theoretical investigations on electrocaloric properties of (111)-oriented $PbMg_{1/3}Nb_{2/3}O_3$ single crystal. J. Adv. Ceram. **2**(4), 308–312 (2013). https://doi.org/10.1007/s40145-013-0076-7
41. M.A. Hamad, Electrocaloric properties of Zr-modified Pb $(Mg_{1/3}Nb_{2/3})O_3$ polycrystalline ceramics. J. Adv. Dielectr. **3**(04), 1350029 (2013). https://doi.org/10.1142/S2010135X1350029X
42. M.A. Hamad, Room temperature giant electrocaloric properties of relaxor ferroelectric 0.93PMN-0.07PT thin film. AIP Adv. **3**(3), 032115 (2013). https://doi.org/10.1063/1.4795156
43. Y. Bai, G.P. Zheng, S.Q. Shi, Mater. Res. Bull. **46**, 1866–1869 (2011)

44. I. Kriaa, N. Abdelmoula, A. Maalej, H. Khemakhem, Study of the electrocaloric effect in the relaxor ferroelectric ceramic 0.75 PMN-0.25 PT. J. Electron. Mater. **44**(12), 4852–4856 (2015). https://doi.org/10.1007/s11664-015-4051-7
45. M.A. Hamad, Investigations on electrocaloric properties of ferroelectric $Pb(Mg_{0.067}Nb_{0.133}Zr_{0.8})O_3$. Appl. Phys. Lett. **102**(14), 142908 (2013). https://doi.org/10.1063/1.4801868
46. S.G. Lu, Q. Zhang, Electrocaloric materials for solid-state refrigeration. Adv. Mater. **21**(19), 1983–1987 (2009). https://doi.org/10.1002/adma.200802902
47. G. Akcay, S.P. Alpay, J.V. Mantese, G.A. Rossetti Jr., Magnitude of the intrinsic electrocaloric effect in ferroelectric perovskite thin films at high electric fields. Appl. Phys. Lett. **90**(25), 252909 (2007). https://doi.org/10.1063/1.2750546
48. H. Chen, T.L. Ren, X.M. Wu, Y. Yang, L.T. Liu, Giant electrocaloric effect in lead-free thin film of strontium bismuth tantalite. Appl. Phys. Lett. **94**(18), 182902 (2009). https://doi.org/10.1063/1.3123817
49. Y. Bai, G.P. Zheng, S.Q. Shi, Abnormal electrocaloric effect of $Na_{0.5}Bi_{0.5}TiO_3$–$BaTiO_3$ lead-free ferroelectric ceramics above room temperature. Mater. Res. Bull. **46**(11), 1866–1869 (2011). https://doi.org/10.1016/j.materresbull.2011.07.038
50. B. Asbani, J.L. Dellis, A. Lahmar, M. Courty, M. Amjoud, Y. Gagou, K. Djellab, D. Mezzane, Z. Kutnjak, M. El Marssi, Lead-free $Ba_{0.8}Ca_{0.2}(Zr_xTi_{1-x})$ O_3 ceramics with large electrocaloric effect. Appl. Phys. Lett. **106**(4), 042902 (2015). https://doi.org/10.1063/1.4906864
51. Y. Zhang, Thermal hysteresis and electrocaloric effect in $Ba_{1-x}Zr_xTiO_3$. J. Phys. Chem. Solids **115**, 326–331 (2018). https://doi.org/10.1016/j.jpcs.2017.12.043
52. Y. Bai, X. Han, L. Qiao, Optimized electrocaloric refrigeration capacity in lead-free (1–x) $BaZr_{0.2}Ti_{0.8}O_{3-x}Ba_{0.7}Ca_{0.3}TiO_3$ ceramics. Appl. Phys. Lett. **102**(25), 252904 (2013). https://doi.org/10.1063/1.4810916
53. B. Zhang, X. Lou, K. Zheng, X. Xie, P. Shi, M. Guo, X. Zhu, Y. Gao, Q. Liu, R. Kang, Enhanced electrocaloric effect in the Sm and Hf co-doped $BaTiO_3$ ceramics. Ceram. Int. **47**(1), 1101–1108 (2021). https://doi.org/10.1016/j.ceramint.2020.08.226
54. S. Liu, Q. Xie, L. Zhang, Y. Zhao, X. Wang, P. Mao, J. Wang, X. Lou, Tunable electrocaloric and energy storage behavior in the Ce, Mn hybrid doped $BaTiO_3$ ceramics. J. Eur. Ceram. Soc. **38**(14), 4664–4669 (2018). https://doi.org/10.1016/j.jeurceramsoc.2018.06.020
55. S. Patel, A. Chauhan, R. Vaish, Multiple caloric effects in $(Ba_{0.865}Ca_{0.135}Zr_{0.1089}Ti_{0.8811}Fe_{0.01})O_3$ ferroelectric ceramic. Appl. Phys. Lett. **107**(4), 042902 (2015). https://doi.org/10.1063/1.4927558
56. Y.S. Kim, J. Yoo, Electrocaloric effect of lead-free (Ba, Ca)(Zr, Ti)O_3 ferroelectric ceramic. J. Electron. Mater. **44**(8), 2555–2558 (2015). https://doi.org/10.1007/s11664-015-3732-6
57. P.D. Thacher, Electrocaloric effects in some ferroelectric and antiferroelectric Pb(Zr, Ti)O_3 compounds. J. Appl. Phys. **39**(4), 1996–2002 (1968). https://doi.org/10.1063/1.1656478
58. M.D. Li, X.G. Tang, S.M. Zeng, Q.X. Liu, Y.P. Jiang, W.H. Li, Giant electrocaloric effect in $BaTiO_3$–Bi $(Mg_{1/2}Ti_{1/2})$ O_3 lead-free ferroelectric ceramics. J. Alloys Compd. **747**, 1053–1061 (2018). https://doi.org/10.1016/j.jallcom.2018.03.102
59. R. Chaim, Densification mechanisms in spark plasma sintering of nanocrystalline ceramics. Mater. Sci. Eng. A **443**(1–2), 25–32 (2007). https://doi.org/10.1016/j.msea.2006.07.092
60. H. Kaddoussi, A. Lahmar, Y. Gagou, B. Asbani, J.L. Dellis, G. Cordoyiannis, B. Allouche, H. Khemakhem, Z. Kutnjak, M. El Marssi, Indirect and direct electrocaloric measurements of $(Ba_{1-x}Ca_x)(Zr_{0.1}Ti_{0.9})O_3$ ceramics (x=0.05, x=0.20). J. Alloys Compd. **667**, 198–203 (2016). https://doi.org/10.1016/j.jallcom.2016.01.159
61. B. Neese, B. Chu, S.G. Lu, Y. Wang, E. Furman, Q.M. Zhang, Large electrocaloric effect in ferroelectric polymers near room temperature. Science **321**(5890), 821–823 (2008). https://doi.org/10.1126/science.1159655
62. M. Zannen, A. Lahmar, Z. Kutnjak, J. Belhadi, H. Khemakhem, M. El Marssi, Electrocaloric effect and energy storage in lead free $Gd_{0.02}Na_{0.5}Bi_{0.48}TiO_3$ ceramic. Solid State Sci. **66**, 31–37 (2017). https://doi.org/10.1016/j.solidstatesciences.2017.02.007
63. V. Franco, J.S. Blázquez, A. Conde, Field dependence of the magnetocaloric effect in materials with a second order phase transition: a master curve for the magnetic entropy change. Appl. Phys. Lett. **89**(22), 222512 (2006). https://doi.org/10.1063/1.2399361
64. V. Franco, A. Conde, Scaling laws for the magnetocaloric effect in second order phase transitions: from physics to applications for the characterization of materials. Int. J. Refrig. **33**(3), 465–473 (2010). https://doi.org/10.1016/j.ijrefrig.2009.12.019
65. M. Bourguiba, M.A. Gdaiem, M. Chafra, E.K. Hlil, H. Belmabrouk, A. Bajahzar, Effect of titanium substitution on the structural, magnetic and magnetocaloric properties of $La_{0.67}Ba_{0.25}Ca_{0.08}MnO_3$ perovskite manganites. Appl. Phys. A **125**(6), 1–16 (2019). https://doi.org/10.1007/s00339-019-2665-y
66. S. Bouzidi, M.A. Gdaiem, J. Dhahri, E.K. Hlil, Large magnetocaloric entropy change at room temperature in soft ferromagnetic manganites. RSC Adv. **9**(1), 65–76 (2019). https://doi.org/10.1039/C8RA09166H
67. L.J. Ding, Critical scaling analysis for displacive-type organic ferroelectrics around ferroelectric transition. Phys. A Stat. Mech. Appl. **471**, 818–824 (2017). https://doi.org/10.1016/j.physa.2016.12.085